Interface engineering and heterometal doping Mo-NiS/Ni(OH)$_2$ for overall water splitting

Hua Zhang[1], Baojuan Xi[1], Yu Gu[1], Weihua Chen[2], and Shenglin Xiong[1] (✉)

[1] Key Laboratory of Colloid and Interface Chemistry, Ministry of Education, School of Chemistry and Chemical Engineering, State Key Laboratory of Crystal Materials, Shandong University, Jinan 250100, China
[2] Key Laboratory of Material Processing and Mold of Ministry of Education, Zhengzhou University, Zhengzhou 450001, China

ABSTRACT

Developing cost-effective, efficient and bifunctional electrocatalysts is vital for both hydrogen evolution reaction (HER) and oxygen evolution reaction (OER) application. The catalytic activity of electrocatalysts could be optimized by reasonable electronic structure regulation and increasing active sites. Herein, we report the design and fabrication of Mo-doped nickel sulfide/hydroxide heterostructures (Mo-NiS/Ni(OH)$_2$) as a multisite water splitting catalyst via straightforward solvothermal and *in-situ* growth strategy. Based on foreign metal doping and interface interaction, the electronic conductivity of heterostructures is improved and the charge transfer kinetics across the interface is promoted, which are demonstrated by the theoretical calculations. Mo-NiS/Ni(OH)$_2$ electrocatalyst is endowed with high electrocatalytic performance for water splitting and remarkable durability in alkaline electrolyte. It exhibits the low overpotential of 186 and 74 mV at 10 mA·cm^{-2} for OER and HER, respectively. Importantly, after continuously working for 50 h, the current densities of HER and OER both show negligible degeneration. Even, the resulting Mo-NiS/Ni(OH)$_2$ better catalyzes water splitting, yielding a current density of 10 mA·cm^{-2} at a cell voltage of 1.5 V and outperforming Pt/C-IrO$_2$ couple (1.53 V). This result demonstrates that transition metal doping and heterogeneous interface engineering are useful means for conventional catalyst design.

KEYWORDS

heterostructure, doping, bifunctional catalyst, overall water splitting

1　Introduction

Along with the global warming and energy shortage, environment-friendly renewable energy is expected to replace fossil fuels [1–3]. Currently, hydrogen attracts great attention by reason of zero carbon emission and ease to fabricate [4–6]. Electrocatalytic water splitting as a technology that large-scale produces hydrogen and oxygen could satisfy the demands of clean and sustainable energy. It involves two half reactions: cathodic hydrogen evolution reaction (HER) and anodic oxygen evolution reaction (OER). Both of the two reactions play a key role to drive water splitting [7, 8]. But the sluggish kinetics and unfavorable energy barriers of HER and OER lead to large overpotentials, which persistently plague their practical application especially in alkaline electrolyte condition [9, 10]. Such plight strongly encourages us to exploit more HER/OER catalysts with lower overpotential. Now, noble-metal-based electrocatalysts are applied as benchmark for water splitting because of high intrinsic activities. Pt-based materials have superior HER performance and Ir/Ru based materials specialize in OER [11–13]. However, high cost and insufficient reserves of noble-metal-based materials hamper their large-scale development. In response, remarkable endeavors have been devoted to searching for low cost alternatives with high stability and brilliant performance for water splitting.

In the past decades, transition-metal based catalysts have been designed to generate the hydrogen and oxygen, such as transition-metal oxides [14, 15], borides [16, 17], nitrides [18, 19], phosphides [20, 21] and chalcogenides [22–24]. Unfortunately, these obtained single-component catalysts cannot contribute to high performance for both hydrogen and oxygen generation because it is difficult to simultaneously regulate the interaction between hydrogen and oxygen intermediates to effectively realize the overall water-splitting [25]. Hence, constructing bifunctional electrocatalysts with remarkable water splitting activity is of significance for energy re-utilization. Numerous strategies have been applied to design electrode structure for efficient bifunctional electrocatalysts, such as atom doping and heterostructure engineering [26, 27]. Foreign atom doping could tune the electronic structure of host catalysts or adjust the chemical environment of original active sites [28]. To date, various catalysts have been developed by transition metal doping. Duan's group reported the Ni single atoms optimized Pt nanowires to enhance the mass activity [29]. Although, the heteroatom doping is a powerful means to increase the electrocatalytic activity, it is difficult to achieve satisfactory results just by the introduction of foreign atoms for water splitting. Hence, establishing the heterogeneous interface materials is also regarded as an effective tactic to build satisfactory bifunctional catalysts, not only able to provide different active sits for H and O intermediates, but also facilitate electron interaction between different components [30, 31]. Up

to now, heterostructures have been designed and demonstrated to promote the efficiency of overall water splitting. Yan et al. designed lattice well-matched NiPS$_3$/Ni$_2$P heterogeneous interface, which exhibited significantly fast kinetics and accelerated electron transfer [32]. Kanatzidis et al. prepared MoS$_2$ and Co$_9$S$_8$ nanosheets attached on Ni$_3$S$_2$ nanorods which were supported on nickel foam (MoS$_2$/Co$_9$S$_8$/Ni$_3$S$_2$/Ni). The hierarchical nanoassembly exposed abundant active sites and higher activity than the corresponding counterparts, i.e., MoS$_2$/Ni$_3$S$_2$/Ni and Co$_9$S$_8$/Ni$_3$S$_2$/Ni [12].

Based on the aforementioned virtues, it is of high significance to design a nanocomposite catalyst which combines the advantages of the atom doping and heterostructure engineering to improve the electrochemical performance. Herein, we proposed a corresponding strategy to synthesize stable and high efficiently bifunctional electrocatalyst. By doping Mo into NiS, the electronic structure and conductivity of NiS could be improved, which has been proved by the calculation of band gap. The Mo-NiS/Ni(OH)$_2$ was prepared by solvothermal method and subsequent room-temperature solution-based reaction. The as-obtained Mo-NiS/Ni(OH)$_2$ shows unique heterostructure which brings about abundant active sites and optimizes the adsorption and desorption of intermediates. Benefiting from element doping and construction of the heterostructure, the Mo-NiS/Ni(OH)$_2$ hybrid exhibits remarkable electrocatalytic performance with the overpotential of 186 mV for OER and 74 mV for HER at the current density of 10 mA·cm^{-2} under alkaline conditions. In addition, the Mo-NiS/Ni(OH)$_2$ worked as the electrode for overall water splitting electrolyzer, only requiring 1.5 V to reach the current density of 10 mA·cm^{-2}, which is superior to most bifunctional electrocatalysts reported. This strategy could encourage the development of novel catalysts of renewable energy sources.

2 Experimental

2.1 Synthesis of electrocatalysts

NiS was synthesized by one step solvothermal method. 1.2 mmol nickel acetate (Ni(CH$_3$COO)$_2$·4H$_2$O) and 2 mmol thiourea (CH$_4$N$_2$S) were added in a mixed solution of 30 mL deionized water and 10 mL monoethanolamine (C$_2$H$_7$NO). After stirring for 30 min, the solution was transferred into a 50 mL Teflon-lined autoclave. The temperature maintained at 160 °C for 12 h. After the autoclave cooled down naturally, the product was collected and washed repeatedly by deionized water, and dried in vacuum at 60 °C overnight.

The synthesis process of Mo-NiS was similar to that of NiS, except that a different amount of sodium molybdate (Na$_2$MoO$_4$·2H$_2$O) was dispersed in the aforementioned mixed solution of nickel acetate and thiourea to get Mo$_x$-NiS.

The NiS/Ni(OH)$_2$ and Mo$_x$-NiS/Ni(OH)$_2$ were synthesized by growing Ni(OH)$_2$ nanoflakes on NiS or Mo$_x$-NiS surface. The as-prepared NiS or Mo$_x$-NiS was dispersed in 50 mL ethanol solution with continuous stirring for 6 h to get NiS/Ni(OH)$_2$ or Mo$_x$-NiS/Ni(OH)$_2$ sample.

2.2 Characterizations

Powder X-ray diffraction (XRD) patterns of the samples were investigated by a Bruker D8 Advance X-ray diffractometer equipped with Cu Kα radiation (λ = 1.5418 Å). The morphology and structure of the as-prepared catalysts were obtained by field-emission scanning electron microscopy (FESEM, GeminiSEM 300) and FEI Talos F200X transmission electron microscopy (TEM) at an acceleration voltage of 200 kV. The element

contents were investigated by inductively coupled plasma mass spectrometry (ICP-MS, PerkinElmer NexION 350). X-ray photoelectron spectroscopy (XPS) analysis was obtained on an X-ray photoelectron spectrometer (Thermo ESCALAB 250Xi) with Al Kα (hv = 1,486.6 eV) as the excitation source.

2.3 Electrochemical measurements

The electrochemical measurements were carried out on a CHIN760E electrochemistry workstation (ChenHua, ShangHai) in a N$_2$-saturated and O$_2$-saturated standard three electrode system with 1 M KOH solution as electrolyzer for HER and OER test. The rotating disk electrode (Pine, USA) worked as working electrode, graphite rod as counter electrode and Ag/AgCl as reference electrode. Before experiments, the potential of the Ag/AgCl reference electrode was regularly calibrated in KCl solution. In general, 10 mg of catalyst sample and 0.5 mg of acetylene black were dispersed in 0.97 mL isopropyl alcohol containing 30 μL Nafion solution (5.0 wt.%) to form comparatively homogeneous catalyst ink after 1.0 h sonication. The loading mass of the catalyst on glassy carbon electrode was 0.5 mg·cm^{-2}. Based on the Nernst equation: $E_{RHE} = E_{Ag/AgCl} + 0.059pH + E^0_{Ag/AgCl}$, the potentials vs. Ag/AgCl of all tests were transformed into reversible hydrogen electrode (RHE). In addition, the polarization curves were performed with *iR*-compensation. Electrochemical impedance spectroscopy (EIS) was conducted in the frequency range of 0.1 Hz–100 kHz. The electrochemical active surface area (ECSA) was measured by double-layer capacitance in the non-faradic current region and calculated from cyclic voltammetry (CV) with the scan rates ranging from 20 to 100 mV·s^{-1}. The overall water splitting was tested in a two-electrode device using Mo-NiS/Ni(OH)$_2$ catalyst as the anode and cathode.

3 Result and discussion

The protocol of fabricating Mo-NiS/Ni(OH)$_2$ contains two step treatments (Fig. 1). Firstly, Mo atoms were introduced to NiS nanorod assembled urchins by solvothermal method to form Mo doped NiS (Mo-NiS). Then the Mo-NiS as precursor was immersed in ethanol solution to grow the Ni(OH)$_2$ nanoflakes outside. The morphology and structure of these materials were characterized by FESEM and TEM. As shown in Figs. 2(a) and 2(b), and Fig. S1(a) in the Electronic Supplementary Material (ESM), the Mo-NiS and NiS have a similar three-dimensional (3D) urchin-like structure with an average diameter of about 1.5 μm. The FESEM images of Mo-NiS/Ni(OH)$_2$ and NiS/Ni(OH)$_2$ are shown in Fig. 2(c) and Fig. S1(b) in the ESM, which reveal thin Ni(OH)$_2$ nanoflakes coating on the periphery of Mo-NiS and NiS to form heterostructures. The mass ratio of Mo and Ni in Mo-NiS/Ni(OH)$_2$ was estimated by ICP-MS in Table S1 in the ESM. The molar ratio of Mo:Ni is about 6:100, so the Mo-NiS/Ni(OH)$_2$ is also denoted as Mo$_{0.06}$-NiS/Ni(OH)$_2$ in the ESM. The SEM images of Mo$_x$-NiS/Ni(OH)$_2$ are shown in Figs. S2(a)–S2(c) in the ESM, which indicates Mo doping has no influence on the final morphology. The TEM images of Mo-NiS/Ni(OH)$_2$ in Figs. 2(d) and 2(e) further show evident morphological and structural distinction between Mo-NiS and Mo-NiS/Ni(OH)$_2$. The heterostructure of Mo-NiS and Ni(OH)$_2$ well produces synergistic interaction at the interface, which favorably provides action for water splitting [20, 25]. The high-resolution TEM (HRTEM) image shows clear lattice fringes of Mo-NiS/Ni(OH)$_2$. In Fig. 2(f), the lattices with *d*-spacings of 0.47 and 0.24 nm accord with the (110) and (101) planes of Mo-NiS and Ni(OH)$_2$, respectively. The boundary of Mo-NiS and Ni(OH)$_2$ could be found clearly. Scanning TEM
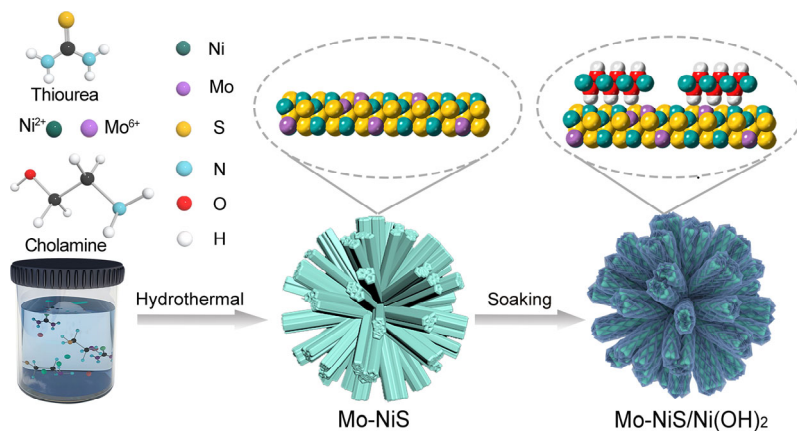
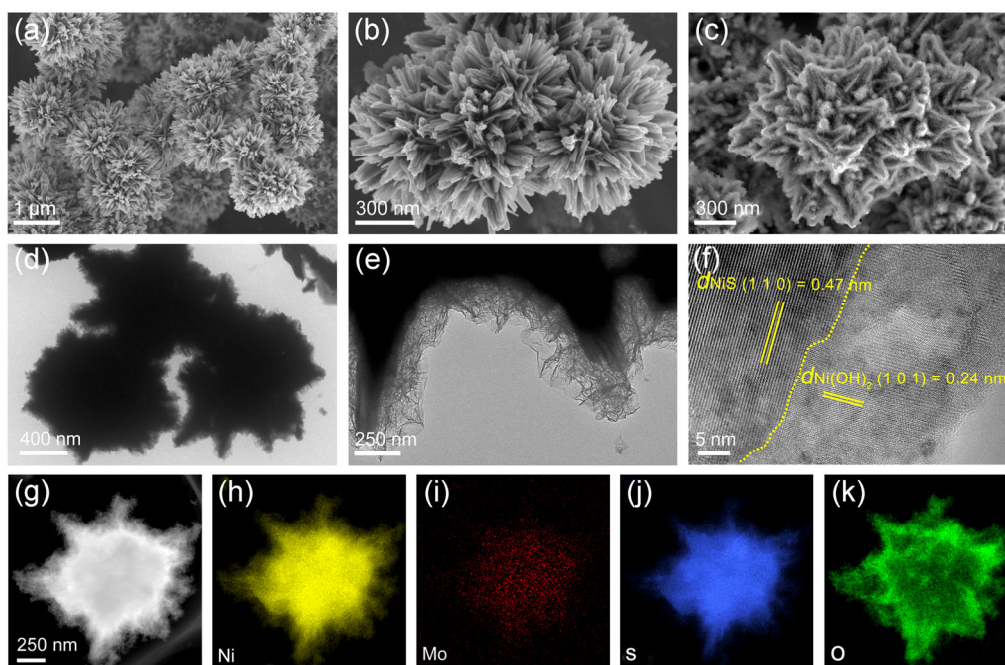**Figure 1** Schematic illustration of preparation of Mo-NiS/Ni(OH)$_2$.

Figure 2 (a) and (b) FESEM images of Mo-NiS. (c) FESEM image of Mo-NiS/Ni(OH)$_2$. (d) and (e) TEM images of Mo-NiS/Ni(OH)$_2$. (f) HRTEM image of Mo-NiS/Ni(OH)$_2$. (g)–(k) STEM-EDX elemental mapping of Mo-NiS/Ni(OH)$_2$.

(STEM) and energy-dispersive X-ray (EDX) elemental mappings display the spatial distribution of Ni, S, O, Mo elements over the Mo-NiS/Ni(OH)$_2$. In Fig. 2(h), the Ni element mapping indicates the dispersion through the entire heterostructure. Figures 2(i) and 2(j) demonstrate the Mo and S are evenly distributed across Mo-NiS. The O element image in Fig. 2(k) could clearly find that Ni(OH)$_2$ nanoflakes are distributed outside of Mo-NiS/Ni(OH)$_2$.

XRD patterns are shown in Fig. 3(a), where the diffraction peaks of NiS are corresponding to NiS (JCPDS No. 12-0041). The XRD peaks of Mo-NiS/Ni(OH)$_2$ and NiS/Ni(OH)$_2$ at 33.4, 34.1 and 45.9 could be attributed to Ni(OH)$_2$ (JCPDS No. 38-0715) and other diffraction peaks are well indexed to NiS (JCPDS No. 12-0041). After Mo doping, peaks do not show obvious shift and no new peaks of Mo sulfides that could be attributed to the low Mo-doping level [27]. In Fig. S2(d) in the ESM, other Mo$_x$-NiS/Ni(OH)$_2$ samples also present the similar diffraction patterns to NiS/Ni(OH)$_2$. XPS analyses were performed to investigate the valence of Ni, S, Mo and O elements in Mo-NiS/Ni(OH)$_2$ and the survey spectrum in Fig. S3 in the ESM also demonstrates the existence of these elements. In Fig. 3(b), the Mo 3d spectral peak at 226.2 eV comes from S 2s orbit. The characteristic peaks at 228.9 and

232.2 eV can be recognized as Mo 3d$_{5/2}$ and Mo 3d$_{3/2}$ of Mo^{4+} in Mo-NiS/Ni(OH)$_2$, suggesting the formation of Mo–S bond. The signals at 232.8 and 234.5 eV correspond to Mo^{6+} species [33–35]. Figure 3(c) shows the high-resolution Ni 2p spectrum of Mo-NiS/Ni(OH)$_2$ displaying two main peaks at 856.5 and 874.3 eV that could be appointed to Ni 2p$_{3/2}$ and Ni 2p$_{1/2}$ of Ni^{3+}. The peaks located at 853.2 and 871.6 eV can be ascribed to Ni^{2+} [36–39]. Compared with the pure NiS, the binding energy of Ni 2p (2p$_{3/2}$ and 2p$_{1/2}$) for NiS/Ni(OH)$_2$ is actively shifted by ≈ 0.30 eV, which manifests that interface effectively regulates the electronic state of NiS. In Fig. 3(d), the S 2p spectrum of NiS/Ni(OH)$_2$ involves S^{2-} with binding energies of 161.4 eV (S 2p$_{3/2}$) and 162.6 eV (S 2p$_{1/2}$). By comparison, the S 2p orbits in pristine NiS have a higher binding energy, suggesting the electronic state changes after interface generation [40, 41]. The Ni 2p and S 2s peaks of Mo-NiS/Ni(OH)$_2$ have different-degree shifts compared with NiS/Ni(OH)$_2$, indicating the Mo doping exerts an effect on the electronic structure of NiS [42].

To dig out the water splitting application, the two related reactions were done with Mo$_x$-NiS/Ni(OH)$_2$ as the electrode. The linear sweep voltametry (LSV) curves of Mo$_x$-NiS/Ni(OH)$_2$ in Fig. S4 in the ESM indicate appropriate Mo doping level
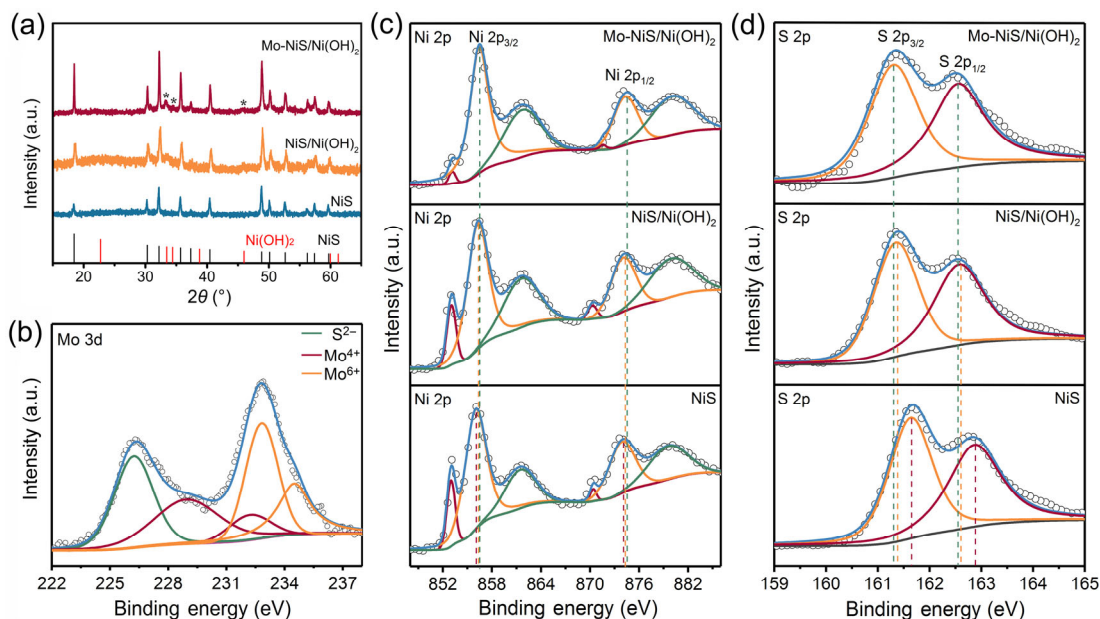
Figure 3 (a) XRD analysis of Mo-NiS/Ni(OH)₂, NiS/Ni(OH)₂ and NiS. XPS results of samples under study: (b) Mo 3d, (c) Ni 2p, (d) S 2s spectra of Mo-NiS/Ni(OH)₂.

could optimize the OER performance. For comparison, the NiS/Ni(OH)₂, NiS and Ir/C were also investigated in duplicated equipment and the corresponding LSV curves are shown in Fig. 4(a). Obviously, the catalytic activity of Mo-NiS/Ni(OH)₂ outperforms NiS/Ni(OH)₂, NiS and even Ir/C catalyst. The onset potential of Mo-NiS/Ni(OH)₂ is only about 1.41 V vs. RHE, which is smaller than that of Ir/C (1.43 V vs. RHE), NiS/Ni(OH)₂ (1.44 V vs. RHE) and NiS (1.49 V vs. RHE). Among these catalysts, Mo-NiS/Ni(OH)₂ also exhibits a low overpotential of 186 mV to reach the current density of 10 mA·cm⁻², which is lower than 237, 322, and 270 mV for NiS/Ni(OH)₂, NiS and commercial Ir/C, respectively. These results verify the heterostructure construction of NiS/Ni(OH)₂ and doping of Mo atoms can well enhance the oxygen generation.

In addition, the Tafel slope analyses deduced from polarization curves provide intensive insight to the OER kinetic process. As shown in Fig. 4(b), the Mo-NiS/Ni(OH)₂ displays a smaller Tafel slope of 23 mV·dec⁻¹ compared with 75 mV·dec⁻¹ of NiS/Ni(OH)₂ and 150 mV·dec⁻¹ of NiS. To gain inherent perception of Mo-NiS/Ni(OH)₂ with excellent OER activity, EIS was used to scrutinize the charge transfer kinetics between the electrolyte and electrode during the oxygen generation process. As shown in the Nyquist plots in Fig. 4(c), the charge transfer resistances (R_{ct}) are about 10.0, 18.5, and 22.0 Ω for Mo-NiS/Ni(OH)₂, NiS/Ni(OH)₂ and NiS, respectively. The low value of R_{ct} means the fast charge transfer velocity of Mo-NiS/Ni(OH)₂. The EIS results consistent with the overpotential and Tafel slope further illustrate Mo-NiS/Ni(OH)₂ has a better OER activity. The excellent performance could be ascribed to the electronic configuration of Mo-NiS/Ni(OH)₂ driven by Mo atoms doping and interface interaction between Mo-NiS and Ni(OH)₂. From the intrinsic perspective, the Ni(OH)₂ nanoflakes on the surface of Mo-NiS could optimize the adsorption and desorption energy barriers of oxygenated intermediates (O*, HO*, and HOO*) [43]. The interface interaction between Ni(OH)₂ and Mo-NiS could tailor the electronic structure of catalysts and further influence the kinetics of OER process, which is a reason for the decrease of overpotential. Such a property is more outstanding than most transition metal-based OER catalysts reported in the documents as show in Table S2 in

the ESM. Furthermore, the ECSA is revealed by the double-layer capacitance (C_{dl}) in Fig. S5 in the ESM. The ECSA of Mo-NiS/Ni(OH)₂ is 130 cm² which is higher than 89 cm² for NiS/(OH)₂ and 25 cm² for NiS, implying Mo-NiS/Ni(OH)₂ has more effective active sites after doping and the formation of Ni(OH)₂ nanoflakes on NiS surface. In order to estimate the improved intrinsic activity of the samples, the current densities of Mo-NiS/Ni(OH)₂, NiS/Ni(OH)₂ and NiS were normalized by ECSA and plotted in Fig. S6 in the ESM. Obviously, Mo-NiS/Ni(OH)₂ owns an outstanding intrinsic OER activity. For the superior OER activity, the stability test is indispensable. The long term stability of Mo-NiS/Ni(OH)₂ was analyzed to certify the excellent stability by means of chronopotentiometry test. Figure 4(g) shows the stability measurement of Mo-NiS/Ni(OH)₂ at the current density of 30 mA·cm⁻² for 50 h without significant degradation, proving the remarkable durability of the Mo-NiS/Ni(OH)₂ catalyst. As shown in Fig. S7 in the ESM, after 2,000 cycles of CV scanning, the LSV curve of Mo-NiS/Ni(OH)₂ shows a slight shift. The ICP measurement after long CV cycles is shown in Table S1 in the ESM, the Ni and Mo contents are maintained. The corresponding FESEM image and XRD pattern of the Mo-NiS/Ni(OH)₂ are shown in Fig. S8 in the ESM. It is clear that the original structure is well-retained. But the Ni(OH)₂ nanoflakes collapse because of surface oxidation. In Fig. S9 in the ESM, the disappearance of the Ni²⁺ peaks at 853.2 and 871.6 eV after CV tests also illustrates the surface oxidation [20, 39].

Then, the behaviors of Mo-NiS/Ni(OH)₂ in the HER reaction were examined for thoroughly understanding its catalytic activity. For comparison, the commercial Pt/C, NiS/Ni(OH)₂ and NiS were also evaluated in N₂-saturated 1M KOH. Similarly, the Mo content was testified by LSV in Fig. S10 in the ESM to figure out the effect on the activity. As show in Fig. 4(d), the polarization curves reveal the electrochemical activity of Mo-NiS/Ni(OH)₂, NiS/Ni(OH)₂ and NiS with Pt/C as the reference. The onset potentials of Mo-NiS/Ni(OH)₂, Mo-NiS, NiS are around 15, 50, and 90 mV, respectively. Clearly, the Mo-NiS/Ni(OH)₂ displays favorable ability for hydrogen generation comparable to Pt/C, which results from the impact of Mo doping and the formation of Ni(OH)₂. As the significant parameter to value the catalyst activity, the overpotential at a
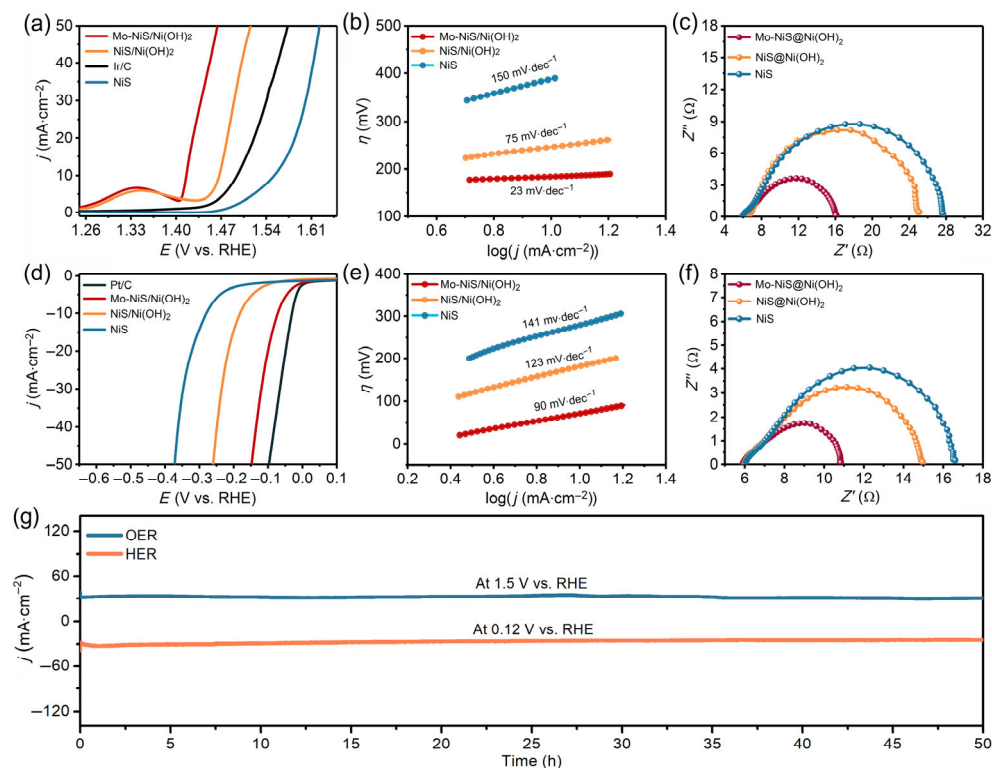
Figure 4 (a) and (d) Polarization curves of OER and HER. (b) and (e) Tafel slopes of as obtained materials. (c) and (f) Nyquist plots of NiS, NiS/Ni(OH)$_2$ and Mo-NiS/Ni(OH)$_2$ with a frequency range of 0.01 Hz to 100 kHz. (g) Stability tests of Mo-NiS/Ni(OH)$_2$ for OER and HER.

current density of 10 mA·cm^{-2} can be derived from polarization curves. The overpotential of Mo-NiS/(OH)$_2$ is 74 mV, much smaller than those of NiS/Ni(OH)$_2$ (182 mV) and NiS (230 mV). What's more, it is lower than lots of already reported none-noble based electrocatalysts in Table S3 in the ESM. To evaluate the HER reaction kinetic parameters, the Tafel slope and exchange current were carried out. Figure 4(e) shows the Tafel slopes of these electrocatalysts. The Mo-NiS/Ni(OH)$_2$ affords a Tafel slope of 90 mV·dec^{-1} in the range of 35–120 mV·dec^{-1}, so the hydrogen generation process is dominated by the Volmer and Heyrovsky step [7, 24]. By comparison, it is more advantageous than NiS/Ni(OH)$_2$ (123 mV·dec^{-1}) and NiS (141 mV·dec^{-1}). The reasons for the improved catalytic activity of Mo-NiS/Ni(OH)$_2$ could be summarized as follows. Ni(OH)$_2$ could interact with OH accelerating water dissociation and Mo-NiS is able to supply H* adsorption sites to promote the H$_2$ formation [34]. Furthermore, the exchange current densities (j_0) are derived from Tafel slope and shown in Fig. S11 in the ESM. The j_0 values are 1.74, 0.3, and 0.11 mA·cm^{-2} for Mo-NiS/Ni(OH)$_2$, NiS/Ni(OH)$_2$ and NiS, respectively. The results of Tafel plot and exchange current density indicate faster reaction kinetic of Mo-NiS/Ni(OH)$_2$ during hydrogen evolution. EIS was also investigated to deepen perception of HER process. The Nyquist plots in Fig. 4(f) display Mo-NiS/Ni(OH)$_2$ with smallest R_{ct} of 5.0 Ω compared with Mo-NiS (9.0 Ω) and NiS (10.5 Ω). It further validates the enhanced charge transfer rate and brilliant conductivity of Mo-NiS/Ni(OH)$_2$. These excellent electrochemical performances could be ascribed to the Mo element doping changing the electronic structure of NiS and strong interface interaction between the core Mo-NiS and the shell Ni(OH)$_2$ [44, 45].

In addition, Fig. S12 in the ESM confirms Mo-NiS/Ni(OH)$_2$ exposes a larger electrochemical surface area and more effective active sites. The polarization curves of Mo-NiS/Ni(OH)$_2$, NiS/Ni(OH)$_2$ and NiS were normalized by electrochemical surface area. The result further proves Mo-NiS/Ni(OH)$_2$ catalyst

displays excellent HER activity compared with other two samples as shown in Fig. S13 in the ESM. Moreover, the durability test of Mo-NiS/Ni(OH)$_2$ in Fig. 4(g), the chronoamperometric measurements for Mo-NiS/Ni(OH)$_2$ at a current density of 30 mA·cm^{-2} present no obvious degradation over 50 h, which indicates the sample has superior stability. As shown in Fig. S14 in the ESM, the polarization curves of Mo-NiS/Ni(OH)$_2$ have slight degradation after 2,000 cycles CV scanning. The morphology and phase investigation after CV cycles measurement in Fig. S15 in the ESM also manifest the excellent structural stability.

According to the aforementioned results, we propose feasible water splitting mechanism of Mo-NiS/Ni(OH)$_2$ in alkaline electrolyte and the schematic illustration is shown in Fig. 5(a). For hydrogen evolution, the Ni(OH)$_2$ nanoflakes accelerate water dissociation and provide active sides for OH$^-$ adsorption. Then, the generated H* species are adsorbed by Mo-NiS and combined to release hydrogen. For oxygen evolution, the OH$^-$ ions from water dissociation and alkaline electrolyte are anchored onto Ni(OH)$_2$ and react with flexible OH$^-$ in alkaline solution to form *OH, *O and *OOH intermediates. These oxygen-containing intermediates further translate into O$_2$. The interface between Mo-NiS and Ni(OH)$_2$ could facilitate the intermediates absorbed on different interfacial sites to boost HER and OER process [25]. Besides, the element doping in NiS could regulate the electronic structure to improve the electronic conductivity of NiS. Based on the superior OER and HER electrocatalytic performance of Mo-NiS/Ni(OH)$_2$, we employed the Mo-NiS/Ni(OH)$_2$ as a bifunctional catalyst to construct a two-electrode electrolytic device for overall water splitting in 1 M KOH solution. The Mo-NiS/Ni(OH)$_2$ supported on nickel foam worked as both electrodes. For comparison, the similar device was assembled which included Pt/C and IrO$_2$/C electrodes as a benchmark. In Fig. 5(b), the polarization curves show the water splitting voltage of 1.50 V for Mo-NiS/Ni(OH)$_2$ to obtain the current density 10 mA·cm^{-2}.
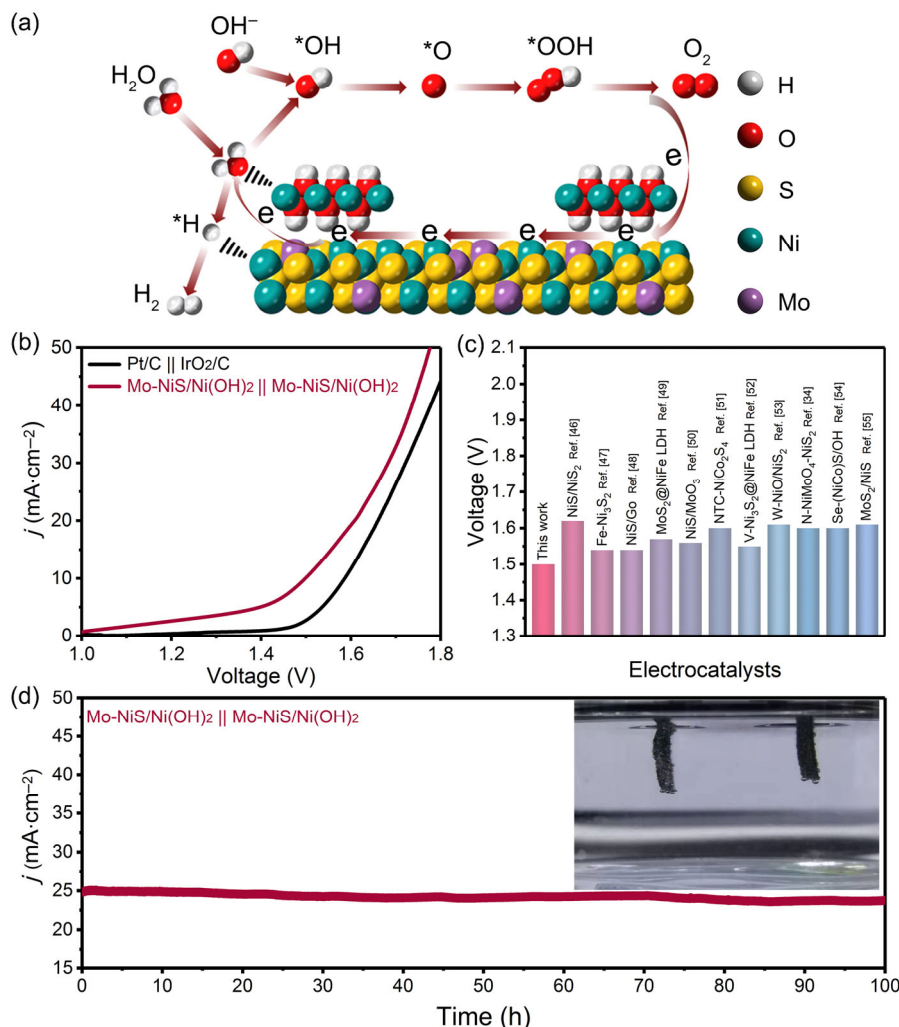
Figure 5 (a) The illustrated water splitting process on Mo-NiS/Ni(OH)$_2$. (b) LSV curves of Mo-NiS/Ni(OH)$_2$ cell and Pt/C-IrO$_2$/C cell. (c) Comparison of cell voltage of different catalysts at the current density of 10 mA·cm^{-2}. (d) Chronopotentiometric measurements of Mo-NiS/Ni(OH)$_2$ at 25 mA·cm^{-2}.

Impressively, the performance of Mo-NiS/Ni(OH)$_2$ couple well surpasses the Pt/C-IrO$_2$/C counterpart at the same current density. In addition, the overall water splitting activity is superior to most transition metal catalysts as shown in Fig. 5(c). What's more, the Mo-NiS/Ni(OH)$_2$ shows robust stability during the overall water splitting process. As presented in Fig. 5(d), after the durability test as long as 100 h, the current density degradation of Mo-NiS/Ni(OH)$_2$ is just about 5%. These results demonstrate Mo-NiS/Ni(OH)$_2$ could replace the noble metal electrocatalysts for alkaline water electrolysis application.

Density functional theory (DFT) calculations were studied to gain deep perception of the catalytic property of Mo-NiS/Ni(OH)$_2$ heterostructure. The optimized heterointerface is consisting of NiS (110) and Ni(OH)$_2$ (001) surface. We calculated the charge density of Mo-NiS/Ni(OH)$_2$ and NiS/Ni(OH)$_2$ to investigate the interaction between two phases at the interface. In Figs. 6(a) and 6(b), the yellow and blue regions represent the charge accumulation and charge depletion, respectively. Obviously, the charge transfer occurs at the interface between NiS and Ni(OH)$_2$, and the obvious charge accumulation on the NiS side indicates the electron transfer from Ni(OH)$_2$ to NiS. The results are consistent with the above mentioned XPS investigations [56, 57]. It should be noted that the charge transfer is obviously intensified after Mo doping in Fig. 6(b), indicating the positive effect on charge transfer. Densities of state (DOS) were also carried out to illustrate the effective electron transfer inside Mo-NiS/Ni(OH)$_2$. As shown in Fig. 6(c),
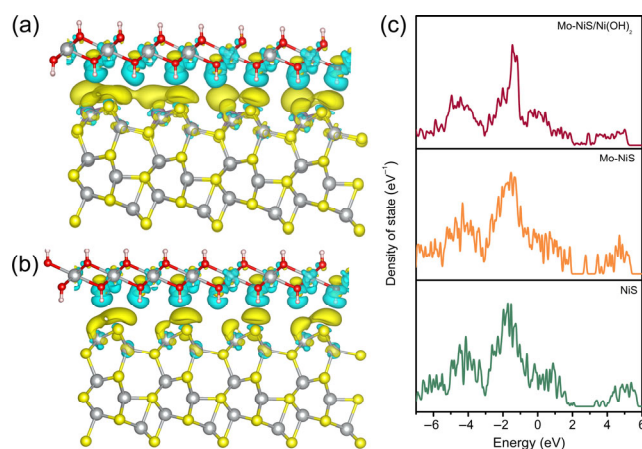

Figure 6 Calculated charge density images of (a) Mo-NiS/Ni(OH)$_2$ and (b) NiS/Ni(OH)$_2$, Ni, S, Mo, O and H atoms are marked in gray, yellow, purple, red, and pink, respectively. (c) Total electronic density of states calculated for Mo-NiS/Ni(OH)$_2$, Mo-NiS and NiS.

the band structure of Mo-NiS/Ni(OH)$_2$ is consecutive near the Fermi level, which demonstrates the intrinsic metallic nature of Mo-NiS/Ni(OH)$_2$ [58]. The band gap reduces after Mo dopingand interface engineering, a token of the improved electrical conductivity. In addition, the charge accumulation on Mo-NiS is favorable for binding H intermediates and the electron depletion of the Ni(OH)$_2$ side is beneficial for

binding oxygen intermediates and displays excellent OER performance [19].

4 Conclusions

In summary, we have synthesized a stable heterostructured Mo-NiS/Ni(OH)₂ by a straightforward solvothermal and *in-situ* growth method. The electrocatalytic activity of Mo-NiS/Ni(OH)₂ is improved by the interface engineering and heteroatom doping. Based on the interface interaction and electronic structure regulating, the as-prepared Mo-NiS/Ni(OH)₂ shows an outstanding OER activity with an overpotential of 186 mV at 10 mA·cm^{-2}, small Tafel slope of about 23 mV·dec^{-1} and superior long-term durability of 50 h at 30 mA·cm^{-2} in 1 M KOH solution. Considering the excellent HER activity, the Mo-NiS/Ni(OH)₂ was evaluated for electrochemical overall water splitting. The assembled water splitting device only needs 1.5 V to achieve the current density of 10 mA·cm^{-2} and presents roust stability for 100 h at 25 mA·cm^{-2}. This work provides a simple way to design transition metal-based materials special for overall water splitting.

References

[1] Dresselhaus, M. S.; Thomas, I. L. Alternative energy technologies. *Nature* **2001**, *414*, 332–337.

[2] Jiao, Y.; Zheng, Y.; Jaroniecb, M.; Qiao, S. Z. Design of electrocatalysts for oxygen- and hydrogen-involving energy conversion reactions. *Chem. Soc. Rev.* **2015**, *44*, 2060–2086.

[3] Shi, Y. M.; Zhang, B. Recent advances in transition metal phosphide nanomaterials: Synthesis and applications in hydrogen evolution reaction. *Chem. Soc. Rev.* **2016**, *45*, 1529–1541.

[4] Gu, Y.; Xi, B. J.; Wei, R. C.; Fu, Q.; Qian, Y. T.; Xiong, S. L. Sponge assembled by graphene nanocages with double active sites to accelerate alkaline her kinetics. *Nano Lett.* **2020**, *20*, 8375–8383.

[5] Turner, J. A. Sustainable hydrogen production. *Science* **2004**, *305*, 972–974.

[6] Symes, M. D.; Cronin, L. Decoupling hydrogen and oxygen evolution during electrolytic water splitting using an electron-coupled-proton buffer. *Nat. Chem.* **2013**, *5*, 403–409.

[7] Zheng, Y.; Jiao, Y.; Vasileff, A.; Qiao, S. Z. The hydrogen evolution reaction in alkaline solution: From theory, single crystal models, to practical electrocatalysts. *Angew. Chem., Int. Ed.* **2018**, *57*, 7568–7579.

[8] Kim, J. S.; Kim, B.; Kim, H.; Kang, K. Recent progress on multimetal oxide catalysts for the oxygen evolution reaction. *Adv. Energy Mater.* **2018**, *8*, 1702774.

[9] Suntivich, J.; May, K. J.; Gasteiger, H. A.; Goodenough, J. B.; Shao-Horn, Y. A perovskite oxide optimized for oxygen evolution catalysis from molecular orbital principles. *Science* **2011**, *334*, 1383–1385.

[10] Vij, V.; Sultan, S.; Harzandi, A. M.; Meena, A.; Tiwari, J. N.; Lee, W. G.; Yoon, T.; Kim, K. S. Nickel-based electrocatalysts for energy-related applications: Oxygen reduction, oxygen evolution, and hydrogen evolution reactions. *ACS Catal.* **2017**, *7*, 7196–7225.

[11] Wei, R. C.; Gu, Y.; Zou, L. L.; Xi, B. J.; Zhao, Y. X.; Ma, Y. N.; Qian, Y. T.; Xiong, S. L.; Xu, Q. Nanoribbon superstructures of graphene nanocages for efficient electrocatalytic hydrogen evolution. *Nano Lett.* **2020**, *20*, 7342–7349.

[12] Yang, Y.; Yao, H. Q.; Yu, Z. H.; Islam, S. M.; He, H. Y.; Yuan, M. W.; Yue, Y. H.; Xu, K.; Hao, W. C.; Sun, G. B. et al. Hierarchical nanoassembly of MoS₂/Co₉S₈/Ni₃S₂/Ni as a highly efficient electrocatalyst for overall water splitting in a wide pH range. *J. Am. Chem. Soc.* **2019**, *141*, 10417–10430.

[13] Zhu, K. K.; Chen, J. Y.; Wang, W. J.; Liao, J. W.; Dong, J. C.; Chee, M. O. L.; Wang, N.; Dong, P.; Ajayan, P. M.; Gao, S. P. et al. Etching-doping sedimentation equilibrium strategy: Accelerating kinetics on hollow Rh-doped CoFe-layered double hydroxides for water splitting. *Adv. Funct. Mater.* **2020**, *30*, 2003556.

[14] Wang, C.; Qi, L. M. Heterostructured inter-doped ruthenium–cobalt oxide hollow nanosheet arrays for highly efficient overall water splitting. *Angew. Chem., Int. Ed.* **2020**, *59*, 17219–17224.

[15] Zhang, L.; Liu, B. R.; Zhang, N.; Ma, M. M. Electrosynthesis of Co₃O₄ and Co(OH)₂ ultrathin nanosheet arrays for efficient electrocatalytic water splitting in alkaline and neutral media. *Nano Res.* **2018**, *11*, 323–333.

[16] Hu, Q.; Li, G. M.; Han, Z.; Wang, Z. Y.; Huang, X. W.; Chai, X. Y.; Zhang, Q. L.; Liu, J. H.; He, C. X. General synthesis of ultrathin metal borate nanomeshes enabled by 3D bark-like N-doped carbon for electrocatalysis. *Adv. Energy Mater.* **2019**, *9*, 1901130.

[17] Dutta, S.; Han, H. S.; Je, M.; Choi, H.; Kwon, H. J.; Park, K.; Indra, A.; Kim, K. M.; Paik, U.; Song, T. Chemical and structural engineering of transition metal boride towards excellent and sustainable hydrogen evolution reaction. *Nano Energy* **2020**, *67*, 104245.

[18] Yao, N.; Li, P.; Zhou, Z. R.; Zhao, Y. M.; Cheng, G. Z.; Chen, S. L.; Luo, W. Synergistically tuning water and hydrogen binding abilities over Co₄N by Cr doping for exceptional alkaline hydrogen evolution electrocatalysis. *Adv. Energy Mater.* **2019**, *9*, 1902449.

[19] Gu, Y.; Chen, S.; Ren, J.; Jia, Y. A.; Chen, C. M.; Komarneni, S.; Yang, D. J.; Yao, X. D. Electronic structure tuning in Ni₃FeN/r-GO aerogel toward bifunctional electrocatalyst for overall water splitting. *ACS Nano* **2018**, *12*, 245–253.

[20] Wu, Y. T.; Wang, H.; Ji, S.; Pollet, B. G.; Wang, X. Y.; Wang, R. F. Engineered porous Ni₂P-nanoparticle/Ni₂P-nanosheet arrays via the Kirkendall effect and Ostwald ripening towards efficient overall water splitting. *Nano Res.* **2020**, *13*, 2098–2105.

[21] Yan, Y. T.; Lin, J. H.; Cao, J.; Guo, S.; Zheng, X. H.; Feng, J. C.; Qi, J. L. Activating and optimizing the activity of NiCoP nanosheets for electrocatalytic alkaline water splitting through the V doping effect enhanced by P vacancies. *J. Mater. Chem. A* **2019**, *7*, 24486–24492.

[22] Feng, L. L.; Yu, G. T.; Wu, Y. Y.; Li, G. D.; Li, H.; Sun, Y. H.; Asefa, T.; Chen, W.; Zou, X. X. High-index faceted Ni₃S₂ nanosheet arrays as highly active and ultrastable electrocatalysts for water splitting. *J. Am. Chem. Soc.* **2015**, *137*, 14023–14026.

[23] Li, H. Y.; Chen, S. M.; Zhang, Y.; Zhang, Q. H.; Jia, X. F.; Zhang, Q.; Gu, L.; Sun, X. M.; Song, L.; Wang, X. Systematic design of superaerophobic nanotube-array electrode comprised of transition-metal sulfides for overall water splitting. *Nat. Commun.* **2018**, *9*, 2452.

[24] Hu, J.; Zhang, C. X.; Jiang, L.; Lin, H.; An, Y. M.; Zhou, D.; Leung, M. K. H.; Yang, S. H. Nanohybridization of MoS₂ with layered double hydroxides efficiently synergizes the hydrogen evolution in alkaline media. *Joule* **2017**, *1*, 383–393.

[25] Li, X. P.; Wang, Y.; Wang, J. J.; Da, Y. M.; Zhang, J. F.; Li, L. L.; Zhong, C.; Deng, Y. D.; Han, X. P.; Hu, W. B. Sequential electrodeposition of bifunctional catalytically active structures in MoO₃/Ni–NiO composite electrocatalysts for selective hydrogen and oxygen evolution. *Adv. Mater.* **2020**, *32*, 2003414.

[26] Yan, Y. T.; Wang, P. C.; Lin, J. H.; Cao, J.; Qi, J. L. Modification strategies on transition metal-based electrocatalysts for efficient water splitting. *J. Energy Chem.* **2021**, *58*, 446–462.

[27] Zhong, W. W.; Wang, Z. P.; Gao, N.; Huang, L. G.; Lin, Z. P.; Liu, Y. P.; Meng, F. Q.; Deng, J.; Jin, S. F.; Zhang, Q. H. et al. Coupled vacancy pairs in Ni-doped CoSe for improved electrocatalytic hydrogen production through topochemical deintercalation. *Angew. Chem., Int. Ed.* **2020**, *59*, 22743–22748.

[28] Pan, Y.; Sun, K. A.; Lin, Y.; Cao, X.; Cheng, Y. S.; Liu, S. J.; Zeng, L. Y.; Cheong, W. C.; Zhao, D.; Wu, K. L. et al. Electronic structure and d-band center control engineering over M-doped CoP (M = Ni, Mn, Fe) hollow polyhedron frames for boosting hydrogen production. *Nano Energy* **2019**, *56*, 411–419.

[29] Li, M. F.; Duanmu, K. N.; Wan, C. Z.; Cheng, T.; Zhang, L.; Dai, S.; Chen, W. X.; Zhao, Z. P.; Li, P.; Fei, H. L. et al. Single-atom tailoring of platinum nanocatalysts for high-performance multifunctional electrocatalysis. *Nat. Catal.* **2019**, *2*, 495–503.

[30] An, L.; Zhang, Z. Y.; Feng, J. R.; Lv, F.; Li, Y. X.; Wang, R.; Lu, M.; Gupta, R. B.; Xi, P. X.; Zhang, S. Heterostructure-promoted oxygen electrocatalysis enables rechargeable zinc–air battery with neutral aqueous electrolyte. *J. Am. Chem. Soc.* **2018**, *140*, 17624–17631.

[31] Zheng, X. R.; Han, X. P.; Cao, Y. H.; Zhang, Y.; Nordlund, D.; Wang, J. H.; Chou, S. L.; Liu, H.; Li, L. L.; Zhong, C. et al. Identifying dense NiSe₂/CoSe₂ heterointerfaces coupled with surface high-valence bimetallic sites for synergistically enhanced oxygen electrocatalysis. *Adv. Mater.* **2020**, *32*, 2000607.

[32] Liang, Q. H.; Zhong, L. X.; Du, C. F.; Luo, Y. B.; Zhao, J.; Zheng, Y.; Xu, J. W.; Ma, J. M.; Liu, C. T.; Li, S. Z. et al. Interfacing epitaxial dinickel phosphide to 2D nickel thiophosphate nanosheets for boosting electrocatalytic water splitting. *ACS Nano* **2019**, *13*, 7975–7984.

[33] Du, C.; Men, Y. N.; Hei, X. Z.; Yu, J. H.; Cheng, G. Z.; Luo, W. Mo-doped Ni₃S₂ nanowires as high-performance electrocatalysts for overall water splitting. *ChemElectroChem* **2018**, *5*, 2564–2570.

[34] An, L.; Feng, J. R.; Zhang, Y.; Wang, R.; Liu, H. W.; Wang, G. C.; Cheng, F. Y.; Xi, P. X. Epitaxial heterogeneous interfaces on N-NiMoO₄/NiS₂ nanowires/nanosheets to boost hydrogen and oxygen production for overall water splitting. *Adv. Funct. Mater.* **2019**, *29*, 1805298.

[35] Jia, Q.; Wang, X. X.; Wei, S.; Zhou, C. L.; Wang, J. W.; Liu, J. Q. Porous flower-like Mo-doped NiS heterostructure as highly efficient and robust electrocatalyst for overall water splitting. *Appl. Surf. Sci.* **2019**, *484*, 1052–1060.

[36] Hung, T. F.; Yin, Z. W.; Betzler, S. B.; Zheng, W. J.; Yang, J.; Zheng, H. M. Nickel sulfide nanostructures prepared by laser irradiation for efficient electrocatalytic hydrogen evolution reaction and supercapacitors. *Chem. Eng. J.* **2019**, *367*, 115–122.

[37] Shang, X.; Zhang, X. Y.; Xie, J. Y.; Dong, B.; Chi, J. Q.; Guo, B. Y.; Yang, M.; Chai, Y. M.; Liu, C. G. Double-catalytic-site engineering of nickel-based electrocatalysts by group VB metals doping coupling with *in-situ* cathodic activation for hydrogen evolution. *Appl. Catal. B Environ.* **2019**, *285*, 117984.

[38] Wang, P. T.; Zhang, X.; Zhang, J.; Wan, S.; Guo, S. J.; Lu, G.; Yao, J. L.; Huang, X. Q. Precise tuning in platinum-nickel/nickel sulfide interface nanowires for synergistic hydrogen evolution catalysis. *Nat. Commun.* **2017**, *8*, 14580.

[39] Luo, X,; Ji, P. X.; Wang, P. Y.; Cheng, R. L.; Chen, D.; Lin, C.; Zhang, J. N.; He, J. W.; Shi, Z. H.; Li, N. et al. Interface engineering of hierarchical branched Mo-doped Ni₃S₂/NiₓPᵧ hollow heterostructure nanorods for efficient overall water splitting. *Adv. Energy Mater.* **2020**, *10*, 1903891.

[40] Zhang, J.; Wang, T.; Pohl, D.; Rellinghaus, B.; Dong, R. H.; Liu, S. H.; Zhuang, X. D.; Feng, X. L. Interface engineering of MoS₂/Ni₃S₂ heterostructures for highly enhanced electrochemical overall-water-splitting activity. *Angew. Chem., Int. Ed.* **2016**, *55*, 6702–6707.

[41] Xiao, X.; Huang, D. K.; Fu, Y. Q.; Wen, M.; Jiang, X. X.; Lv, X. W.; Li, M.; Gao, L.; Liu, S. S.; Wang, M. K. et al. Engineering NiS/Ni₂P heterostructures for efficient electrocatalytic water splitting. *ACS Appl. Mater. Interfaces* **2018**, *10*, 4689–4696.

[42] Wang, L. G.; Duan, X. X.; Liu, X. J.; Gu, J.; Si, R.; Qiu, Y.; Qiu, Y. M.; Shi, D. E.; Chen, F. H.; Sun, X. M. et al. Atomically dispersed Mo supported on metallic Co₉S₈ nanoflakes as an advanced noble-metal-free bifunctional water splitting catalyst working in universal pH conditions. *Adv. Energy Mater.* **2020**, *10*, 1903137.

[43] Lv, L.; Chang, Y. X.; Ao, X.; Li, Z. S.; Li, J. G.; Wu, Y.; Xue, X. Y.; Cao, Y. L.; Hong, G.; Wang, C. D. Interfacial electron transfer on heterostructured Ni₃Se₄/FeOOH endows highly efficient water oxidation in alkaline solutions. *Mater. Today Energy* **2020**, *17*, 100462.

[44] Xu, Q. C.; Jiang, H.; Zhang, H. X.; Hu, Y. J.; Li, C. Z. Heterogeneous interface engineered atomic configuration on ultrathin Ni(OH)₂/Ni₃S₂ nanoforests for efficient water splitting. *Appl. Catal. B Environ.* **2019**, *242*, 60–66.

[45] Zhang, H. J.; Li, X. P.; Hähnel, A.; Naumann, V.; Lin, C.; Azimi, S.; Schweizer, S. L.; Maijenburg, A. W.; Wehrspohn, R. B. Bifunctional heterostructure assembly of NiFe LDH nanosheets on NiCoP nanowires for highly efficient and stable overall water splitting. *Adv. Funct. Mater.* **2018**, *28*, 1706847.

[46] Li, Q.; Wang, D. W.; Han, C.; Ma, X.; Lu, Q. Q.; Xing, Z. C.; Yang, X. R. Construction of amorphous interface in an interwoven NiS/NiS₂ structure for enhanced overall water splitting. *J. Mater. Chem. A.* **2018**, *6*, 8233–8237.

[47] Zhang, G.; Feng, Y. S.; Lu, W. T.; He, D.; Wang, C. Y.; Li, Y. K.; Wang, X. Y.; Cao, F. F. Enhanced catalysis of electrochemical overall water splitting in alkaline media by Fe doping in Ni₃S₂ nanosheet arrays. *ACS Catal.* **2018**, *8*, 5431–5441.

[48] Zhang, D. L.; Mou, H. Y.; Lu, F.; Song, C. X.; Wang, D. B. A novel strategy for 2D/2D NiS/graphene heterostructures as efficient bifunctional electrocatalysts for overall water splitting. *Appl. Catal. B Environ.* **2019**, *254*, 471–478.

[49] Xiong, P.; Zhang, X. Y.; Wan, H.; Wang, S. J.; Zhao, Y. Z.; Zhang, J. Q.; Zhou, D.; Gao, W. C.; Ma, R. Z.; Sasaki, T. et al. Interface modulation of two-dimensional superlattices for efficient overall water splitting. *Nano Lett.* **2019**, *19*, 4518–4526.

[50] Jin, L. J.; Xu, H.; Wang, C.; Wang, Y.; Shang, H. Y.; Du, Y. K. Multi-dimensional collaboration promotes the catalytic performance of 1D MoO₃ nanorods decorated with 2D NiS nanosheets for efficient water splitting. *Nanoscale* **2020**, *12*, 21850–21856.

[51] Li, F.; Xu, R. C.; Li, Y. M.; Liang, F.; Zhang, D. F.; Fu, W. F.; Lv, X. J. N-doped carbon coated NiCo₂S₄ hollow nanotube as bifunctional electrocatalyst for overall water splitting. *Carbon* **2019**, *145*, 521–528.

[52] Zhou, J. Q.; Yu, L.; Zhu, Q. C.; Huang, C. Q.; Yu, Y. Defective and ultrathin NiFe LDH nanosheets decorated on V-doped Ni₃S₂ nanorod arrays: A 3D core–shell electrocatalyst for efficient water oxidation. *J. Mater. Chem. A* **2019**, *7*, 18118–18125.

[53] Wang, H. H.; Liu, T.; Bao, K.; Cao, J.; Feng, J. C.; Qi, J. L. W doping dominated NiO/NiS₂ interfaced nanosheets for highly efficient overall water splitting. *J. Colloid Interface Sci.* **2020**, *562*, 363–369.

[54] Hu, C. L.; Zhang, L.; Zhao, Z. J.; Li, A.; Chang, X. X.; Gong, J. L. Synergism of geometric construction and electronic regulation: 3D Se-(NiCo)Sₓ/(OH)ₓ nanosheets for highly efficient overall water splitting. *Adv. Mater.* **2018**, *30*, 1705538.

[55] Zhai, Z. J.; Li, C.; Zhang, L.; Wu, H. C.; Zhang, L.; Tang, N.; Wang, W.; Gong, J. L. Dimensional construction and morphological tuning of heterogeneous MoS₂/NiS electrocatalysts for efficient overall water splitting. *J. Mater. Chem. A* **2018**, *6*, 9833–9838.

[56] Hua, L. Y.; Zeng, X.; Wei, X. Q.; Wang, H. J.; Wu, Y.; Gu, W. L.; Shi, L.; Zhu, C. Z. Interface engineering for enhancing electrocatalytic oxygen evolution of NiFe LDH/NiTe heterostructures. *Appl. Catal. B Environ.* **2020**, *273*, 119014.

[57] Xue, Z. Q.; Li, X.; Liu, Q. L.; Cai, M. K.; Liu, K.; Liu, M.; Ke, Z. F.; Liu, X. L.; Li, G. Q. Interfacial electronic structure modulation of NiTe nanoarrays with NiS nanodots facilitates electrocatalytic oxygen evolution. *Adv. Mater.* **2019**, *31*, 1900430.

[58] Zhang, R.; Huang, J.; Chen, G. L.; Chen, W.; Song, C. S.; Li, C. R.; Ostrikov, K. *In situ* engineering bi-metallic phospho-nitride bi-functional electrocatalysts for overall water splitting. *Appl. Catal. B Environ.* **2019**, *254*, 414–423.